RESEARCH ARTICLE

Key Points:
- CTIDs are significantly larger in southeast direction due to effect of geomagnetic field and the nature of coseismic surface deformation
- Southward CTIDs split into fast (~2.4–1.7 km/s) and slow (680–520 m/s) modes at ~800 km, however, much slower than the surface Rayleigh wave
- Direct evidence for CTIDs propagating at F_2 layer peak altitudes (~300–440 km) detected from COSMIC radio occultation observations

Correspondence to:
S. Tulasi Ram,
tulasi@iigs.iigm.res.in

Coseismic Traveling Ionospheric Disturbances during the M_w 7.8 Gorkha, Nepal, Earthquake on 25 April 2015 From Ground and Spaceborne Observations

S. Tulasi Ram[1] , P. S. Sunil[1] , M. Ravi Kumar[1], S.-Y. Su[2] , L. C. Tsai[2,3], and C. H. Liu[4]

[1]Indian Institute of Geomagnetism, Navi Mumbai, India, [2]Centre for Space and Remote Sensing Research, National Central University, Chung-Li, Taiwan, [3]GPS Science and Application Research Center, National Central University, Chung-Li, Taiwan, [4]Academia Sinica, Taipei, Taiwan

Abstract Coseismic traveling ionospheric disturbances (CTIDs) and their propagation characteristics during M_w 7.8 Gorkha earthquake in Nepal on 25 April 2015 have been investigated using a suite of ground-based GPS receivers and broadband seismometers along with the spaceborne radio occultation observations over the Indian subcontinent region. Depletion in vertical total electron content, a so called ionospheric hole, is observed near the epicenter ~9–11 min after the onset of earthquake. A positive pulse preceding the depletion, similar to N-shaped perturbation, propagating with an apparent velocity of ~2.4 km/s is observed on the south. Further, the CTIDs in the southward direction are found to split in to fast (~2.4–1.7 km/s) and slow (~680–520 m/s) propagating modes at epicentral distances greater than ~800 km. However, the velocities of fast mode CTIDs are significantly smaller than the surface Rayleigh wave velocity (~3.7 km/s), indicating that they are not the true imprint of Rayleigh wave, instead, can probably be attributed to the superimposed wave front formed by the mixture of acoustic waves excited by main shock and propagating Rayleigh wave. The southward CTIDs are found to propagate at F_2 region altitudes of ~300–440 km captured by Constellation Observing System for Meteorology, Ionosphere and Climate radio occultation observations. The CTIDs with periods of ~4–6 min are observed in all directions with significantly larger amplitudes and faster propagation velocities in south and east directions. The observed azimuthal asymmetry in the amplitudes and velocities of CTIDs are discussed in terms of the alignment with geomagnetic field and nature of surface crustal deformation during the earthquake.

Plain Language Summary The sudden piston-like movement of Earth's surface during earthquakes causes air perturbations (acoustic waves) in the atmosphere which can travel to greater heights in the Earth's atmosphere. In this study, the earthquake-induced acoustic waves were detected at ionospheric altitudes of 300–440 km from the Earth's surface. The waves observed in the upper atmosphere often provide useful information about the nature of Earth's surface breakups and the direction of destruction propagated during the earthquakes. Therefore, tracing of earthquake induced waves in upper atmosphere is a novel tool with many applications in earthquake studies and helpful to predict tsunamis.

1. Introduction

The coupled ionosphere-thermosphere system significantly responds to various forces above from Sun and below from lower atmosphere as well as crustal deformations in the lithosphere. During the large earthquakes, the sudden release of energy due to piston-like coseismic displacement of ground surface launches acoustic waves in to atmosphere, which may form shocks as they propagate upward, due to amplification by the exponential decay of the background atmospheric density. The oscillation of neutrals by these waves sets the ionospheric plasma into motion, via collisions, thus causing ion and electron density perturbations. The amplitudes of ion density perturbations due to earthquakes are rather small compared to the disturbances induced by the geomagnetic storms and other solar driven energetic events. However, the study of coseismic ionospheric disturbances has a great academic value to understand the lithosphere-atmosphere-ionosphere coupling processes, and the tracing of earthquake and tsunami induced waves in the upper atmosphere is an emerging tool with promising applications. The perturbations in ionospheric plasma density during large earthquakes have been widely reported in the literature using both ground-based and spaceborne observations (Astafyeva et al., 2009; Calais & Minster, 1995; Coisson et al., 2015; Liu et al., 2006; Otsuka et al., 2006; Tsugawa et al., 2011, and references therein). The ionospheric total electron content (TEC) observations
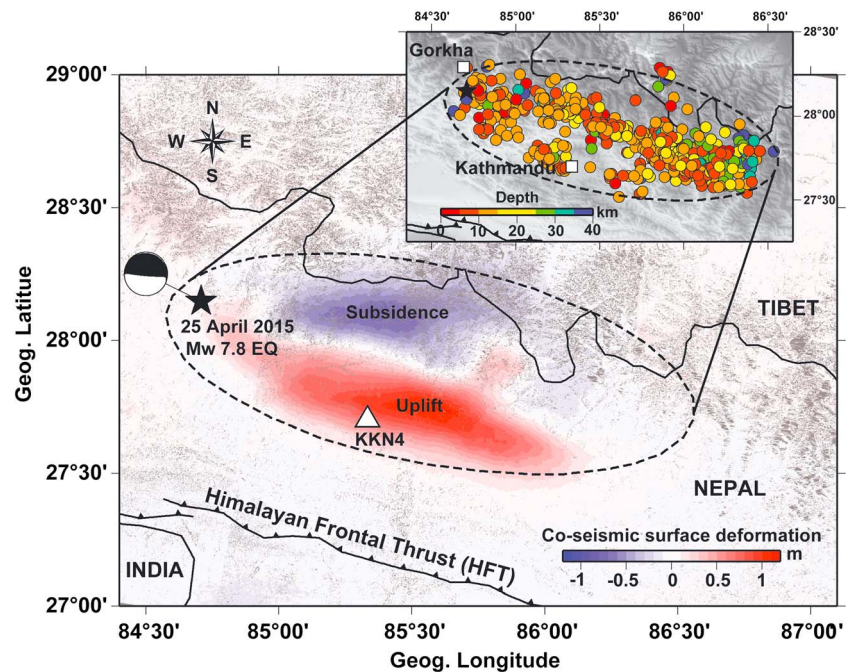
Figure 1. Map illustrates the epicenter location (black star) of 25 April 2015 (M_w 7.8) Gorkha, Nepal earthquake and coseismic surface deformation map generated from Interferometric synthetic aperture radar (InSAR) after Lindsey et al. (2015). The beach ball indicates the thrust faulting as focal mechanism solution. The Himalayan Frontal Thrust (HFT) fault is shown as thin black line with triangles. The inset represents the rupture area with circles indicating the aftershocks of the main event at depth in color scale.

from the ground-based GPS (Global Positioning Systems) receivers are most commonly used because of their accurate and time continuous observations at high temporal resolution as well as the availability of spatially dense and distributed networks (Astafyeva et al., 2009; Dučić et al., 2003; Heki & Ping, 2005; Kakinami et al., 2013; Otsuka et al., 2006; Saito et al., 2011, and references therein).

An earthquake of M_w 7.8 that occurred on 25 April 2015 at 06:11:26 UTC in Gorkha, Nepal, with epicenter located at 28.147°N latitude and 84.708°E longitude caused a catastrophe in central Nepal. The underthrusting of Indian lithosphere beneath the Himalayas makes the Indian and Nepal-Himalayan region vulnerable for earthquakes and seismic hazards. The Gorkha earthquake, which was the largest event in the region since 1934 (Bihar-Nepal) ruptured about 150 km toward east direction of the main shock in Main Himalaya Thrust (MHT), a detachment boundary between India and Eurasian plates which extends to the surface at Himalayan Frontal Thrust (HFT) (Figure 1). Joint inversion of teleseismic, geodetic, and waveform data sets suggests that the rupture front velocity of 3.3 km/s controlled the timing of the rupture propagation toward southeast direction (Kobayashi et al., 2016; Koketsu et al., 2016). The maximum coseismic slip due to thrust faulting occurred at the hypocenter was about 5.7 m at a depth of ~12 km (Sreejith et al., 2016). The surface deformations observed from coseismic InSAR (interferometric synthetic aperture radar) interferograms and ground-based GPS observations show an uplift of ~1–1.3 m near Khatmandu (central Nepal) and a subsidence of ~0.5–0.8 m on the northern region of Nepal as shown in Figure 1 (after Lindsey et al., 2015).

Recent studies have made early reports on the coseismic ionospheric disturbances observed from ground-based GPS receivers (Reddy & Seemala, 2015; Catherine et al., 2016; Sunil et al., 2017; Chen et al., 2016) and satellite observations (Sun et al., 2016) during this Nepal Gorkha earthquake over Indian subcontinent region. Reddy and Seemala (2015) have studied coseismic ionospheric TEC perturbations and reported that the induced TEC perturbations are due to two modes, namely, shock acoustic wave and surface Rayleigh wave-induced perturbations. They have further reported that the average propagation velocity of induced TEC perturbations due to shock acoustic wave and Rayleigh wave is ~1180 m/s and 2400 m/s, respectively. Catherine et al. (2016) have reported east-west
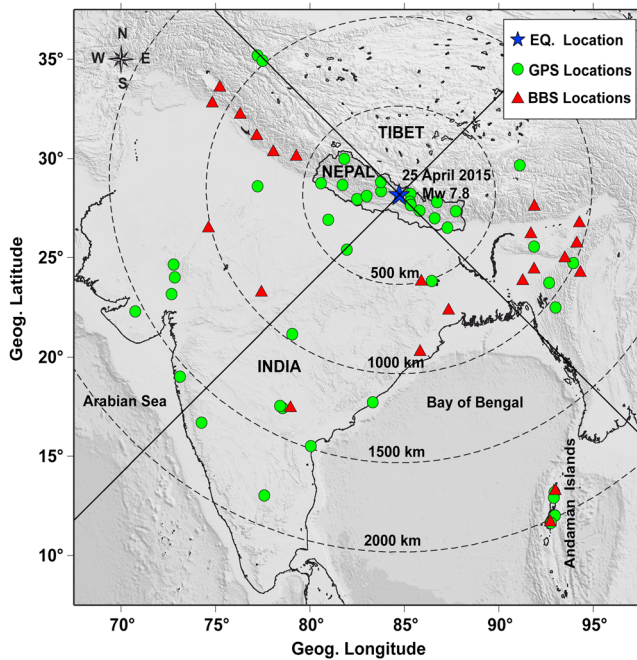
Figure 2. The spatial distribution of ground-based GPS receivers (green circles) and broadband seismometers (red triangles) considered in this study. The blue star indicates the location of epicenter.

asymmetry in the initial arrival time of coseismic ionospheric TEC perturbations. They have also mentioned that the TEC perturbations are predominantly in the east and southeast directions and completely absent in the north of epicenter. Catherine et al. (2016) have also reported the propagation velocity of induced TEC perturbations as 2.6 km/s from the far field GPS stations which they attributed to Rayleigh wave corroborating with that of Reddy and Seemala (2015). However, they have not compared with the surface Rayleigh wave group velocity from the ground-based seismometers during this earthquake event. Recently, Sun et al. (2016) have reported that the earthquake-induced air perturbations uplifted the F_2 layer peak height (h_mF_2) by about 34.4 km within 0.5 to 1 min with an upward velocity of ~573–1,147 m/s using Constellation Observing System for Meteorology, Ionosphere and Climate (COSMIC) radio occultation observations.

The multi-instrumental observations of crustal deformation and Rayleigh wave propagation at surface and the corresponding perturbations in the ionospheric plasma using GPS receivers and space-borne observations provide more comprehensive understanding. Hence, in this paper, apart from the comparison of information from the surface Rayleigh wave group velocity, we further investigate the coseismic traveling ionospheric disturbances (CTIDs) during the Nepal Gorkha earthquake. The characteristics of observed CTIDs are studied in relationship with the nature of crustal deformations by integrating data from ground-based GPS, teleseismic waveform data along with spaceborne GPS radio occultation observations, and the responsible mechanisms are discussed.

2. Data

The TEC observations from the ground-based GPS receivers over Nepal and Indian subcontinent region from Indian Global Navigation Satellite Systems and Nepal Geodetic networks were employed to detect the CTIDs. The 30 s data in RINEX (Receiver INdependent EXchange) format from about 40 GPS receivers are analyzed to derive the vertical TEC (VTEC). The TEC is derived using both code and phase measurements at L1 (1.575 GHz) and L2 (1.227 GHz) frequencies and by accounting differential satellite biases (published by University of Bern) and receiver biases by minimizing TEC variability at predawn hours (Rama Rao et al., 2006; Seemala & Valladares, 2011). The derived line-of-sight TEC values are transformed into VTEC by considering an effective ionospheric shell height of 300 km (Mannucci et al., 1993), and the ionospheric piercing point (IPP) locations corresponding to 300 km height penetration point are noted. In the present analysis, the TEC observations with satellite elevation angles greater than 25° were only considered to avoid multipath effects.

About 22 broadband seismometers (BBS) spanning over the Indian subcontinent region were also examined to estimate the group velocity of surface Rayleigh wave propagation at different azimuthal directions. The vertical component (Z component) of BBS data is only considered in this analysis. It should be mentioned here that the BBS data collected under Indian seismic network by various agencies were not calibrated to common amplitude scale. Hence, the comparison of amplitude of vertical displacement among different stations is not appropriate. Therefore, we considered only the arrival times of Rayleigh waves at different locations in order to estimate the group velocity of surface Rayleigh waves during this M_w 7.8 earthquake.

For example, Figure 2 shows the spatial distribution of ground-based observations considered in this study. The station codes and the geographic locations of GPS receivers and BBS are provided in Table 1. The green circles and red triangles represent the ground-based GPS receivers and BBS locations, respectively. The blue star indicates the location of earthquake epicenter. Further, two vertical electron density profiles from GPS RO (radio occultation) observations of Formosat-3/COSMIC mission over Indian region on 24 and 25 April 2015 were also considered in this study in comparison with ground-based GPS observations.

Table 1

Geographic Locations of Ground-Based GPS Receivers and Broadband Seismometers Used in This Study

Station code	Latitude (°N)	Longitude (°E)
	GPS receivers	
AIZW	23.73	92.66
ALH	25.41	81.94
BASE	35.18	77.22
BMCL	28.66	81.71
BRN2	26.52	87.27
CHLM	28.21	85.31
DELH	28.59	77.22
DGPR	13.18	92.93
DHAN	23.82	86.44
DHAR	24.01	72.84
DNGD	28.75	80.58
DNSG	28.35	83.76
GRHI	27.95	82.49
HAVE	12.01	92.96
HYDE	17.42	78.55
IISC	13.02	77.57
IMPL	24.73	93.93
INCO	17.53	78.4
ISRR	23.16	72.67
JMSM	28.81	83.74
KKN4	27.8	85.28
KOLH	16.68	74.26
LCK3	26.91	80.96
LHAZ	29.66	91.1
MBDR	12.91	92.9
MUMB	19.01	73.11
NAGP	21.14	79.05
NAST	27.66	85.33
ONGO	15.5	80.04
PBRI	11.64	92.71
PORT	11.64	92.74
PYUT	28.1	82.99
RAJK	22.29	70.74
RMTE	26.99	86.6
SAIH	22.49	92.99
SASO	34.92	77.48
SHIL	25.56	91.86
SIPU	24.65	72.78
SMKT	29.97	81.81
SNDL	27.38	85.8
SYBC	27.81	86.71
TPLJ	27.35	87.71
VISA	17.72	83.32
	Broadband seismometers	
AGT	91.26	23.83
AJM	74.63	26.48
BHPL	77.42	23.24
BOKR	85.88	23.79
BRSN	79.27	30.09
BWNR	85.82	20.25
DDI	78.06	30.32
DGPR	92.98	13.25
DHRM	76.3	32.2
DORU	75.23	33.57
HYDE	78.96	17.42
IITK	87.33	22.33
JMU	74.83	32.78
JORH	94.25	26.74

3. Results

It can be observed from the Figure 2, there are eight broadband seismometers (BBS) available in the east (azimuth angle between 45° and 135°), six in the south (azimuth angle between 135° and 225°), and eight in the west (azimuth angle between 225° and 315°). The vertical component of surface displacement observed from these BBS in the east, south, and west directions are shown in Figures 3a–3c, respectively, as a function of time from the onset of earthquake on X axis and epicentral distance on Y axis. As mentioned earlier, these BBS are operated by different agencies over Indian region and were not calibrated to common amplitude scale. Hence, the comparison of Rayleigh wave amplitudes in vertical displacement among different stations is not appropriate. Therefore, only the normalized waveform data of vertical displacements are presented in Figure 3. The normalized waveforms of each station are computed by dividing the vertical displacement with the maximum amplitude in a given time (06–07 UT) as described in appendix. After the arrival of primary and secondary seismic waves, the large amplitudes in vertical displacements indicate the arrival of surface Rayleigh waves (see appendix for identification of Rayleigh waves from the BBS waveform data of vertical displacement). From Figure 3, it can be observed that the Rayleigh waves propagated in all directions. Based on the arrival times of Rayleigh waves at stations with different epicentral distances, the group velocity of surface Rayleigh wave is estimated to be approximately 3.5 km/s in the east and ~3.7 km/s in the south and ~3.4 km/s in the west directions during this Gorkha, Nepal, earthquake. These surface Rayleigh wave velocities estimated using ground-based seismometers are different from the map of Rayleigh wave group velocities presented in Figure 6 of Reddy and Seemala (2015). It should be noted that Reddy and Seemala (2015) have not estimated the surface Rayleigh wave group velocity using ground-based seismometers during this Gorkha, Nepal, earthquake. Instead, they have reproduced the composite map of 10 s period Rayleigh wave velocity from Acton et al. (2010) and compared with the CTID propagation speeds. The map of Acton et al. (2010) represents an average picture of Rayleigh wave group velocities over that region which can be different for individual events.

The initial ionospheric TEC perturbations observed at locations close to the epicenter (within 150 km radius) are shown in Figure 4. Figure 4a shows the locations of epicenter (red star) and the locations of GPS stations ALH, CHLM, NAST, DNSG, and PYUT (solid circles in color). The solid curves in color represent the IPP tracks from the respective stations which are progressing from south to north during this period. The numbers against the station names (see legend) indicate the PRNs of GPS satellites. The thin black lines connecting the GPS stations (colored circles) and the respective IPP tracks (colored curves) indicate the ground projection of line-of-sight (LOS) path at the time of TEC perturbations observed (shown in Figure 4d). Figure 4b shows the VTEC observations from the above stations during 0500–0800 UT. The VTEC observations from these stations are arranged by shifting with a constant offset to avoid the overlapping of the curves for better visibility. The vertical black line indicates the time of earthquake onset. The VTEC from all the stations exhibit similar background variation with a gradual increase from 0500 UT, reaching a maximum around

Table 1 (continued)

Station code	Latitude (°N)	Longitude (°E)
	GPS receivers	
KOHI	94.11	25.72
MORE	94.3	24.24
PBRI	92.72	11.67
SHLG	91.86	24.41
SMLA	77.17	31.13
TAME	93.48	24.98
TAWA	91.87	27.58
UWA	91.69	26.19

0630 UT and again decrease gradually with time. This background variation in VTEC includes both temporal variability as the local time varies from forenoon to afternoon during 0500–0800 UT (~1130 to 1330 LT) and spatial variability as the IPP locations progressing from south to north across the usual equatorial ionization anomaly crest region (not shown in figure) during this period. The VTEC from all the stations exhibits small amplitude wave-like variations of ~12–15 min periods prior to the onset of earthquake during ~0500–0600 UT. These small amplitude wave-like variations prior to the onset of earthquake are appear to be typical ambient gravity waves; however, they have not studied here and could be interesting for further investigation in future studies.

Figures 4c and 4d are same as Figures 4a and 4b, respectively, however shown in enlarged scale for 30 min duration from the onset of earthquake for careful examination of TEC perturbations after the onset of earthquake. The first perturbation in TEC is detected from CHLM-16 in the east as depletion in TEC after 573 s (9.5 min) from the onset of earthquake. The locations of these initial perturbations in TEC are indicated as black open circles over the IPP tracks in Figure 4c. It can be observed from Figures 4c and 4d that the stations in the east (CHLM-16 and NAST-16) detected the TEC perturbations slightly earlier (573 s and 588 s) than the stations in the west (DNSG-16 at 633 s and PYUT-16 at 678 s). Nevertheless, the time period of 573–678 s (~9.5–11 min) is consistent with the velocity of acoustic waves in the atmosphere to reach the ionospheric altitudes of ~300 km. Further, the stations near the epicenter at both east and west detected the initial perturbation as depletion in TEC. The TEC from ALH-26 in south also exhibited depletion in TEC with larger amplitude, however, with an initial positive pulse preceding the depletion as indicated by red arrow in Figure 4b. The duration of initial depleted TEC phase lasts for approximately 240–300 s (4–5 min). However, it is difficult to accurately determine the duration of TEC depletion phase as there are multiple features superposed as discussed later. Therefore, from the observations in Figure 4, one can conclude that the acoustic waves launched by the earthquake initially caused depletion in ionospheric VTEC near the epicenter, with a prior positive pulse in the southward direction. Similar depletion in TEC near epicenter (ionospheric hole) is also observed during the M 9.0 Tohoku-oki earthquake in Japan on 11 March 2011 (Kakinami et al., 2012; Saito et al., 2011; Tsugawa et al., 2011). However, the TEC depletion observed during Tohoku-oki earthquake is significantly large (~3–4 TEC units) and lasted for more than 30 min. Kakinami et al. (2012) have attributed this long lasting TEC depletion (ionospheric hole) to the downwelling of sea surface because of tsunami generation and mentioned that similar ionospheric hole may not occur during inland earthquakes. However, Astafyeva et al. (2013) have argued that "hole" represents the rarefaction (recovery) phase of the N-shaped TEC perturbation due to nonlinear interactions of acoustic waves and expected similar depletions during inland earthquakes of sufficient magnitude. Astafyeva et al. (2013) have also demonstrated that the duration of ionospheric hole increases with the earthquake magnitude. Later, Kamogawa et al. (2015) have compared the TEC perturbations during both submarine and inland earthquakes and concluded that inland earthquakes of sufficiently large magnitude, such as the current Nepal earthquake, can induce ionospheric holes. Recently, Zettergren et al. (2017) have demonstrated through model simulations that the amplitude and duration of TEC depletions varies with the amplitude of the ocean surface responses to the earthquake. Therefore, the TEC depletion observed near the epicenter (Figure 4) can be attributed to the so called "ionospheric hole" due to nonlinear interaction of acoustic
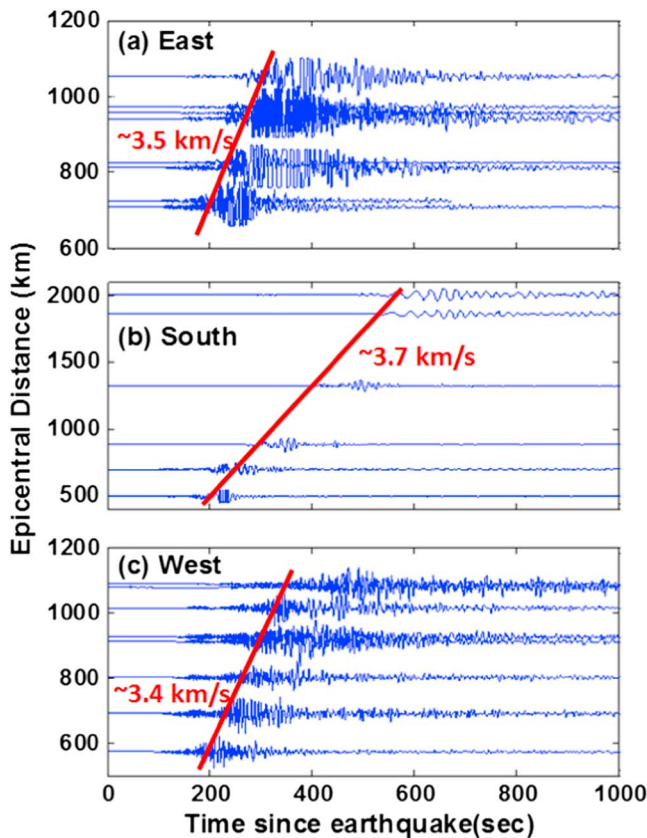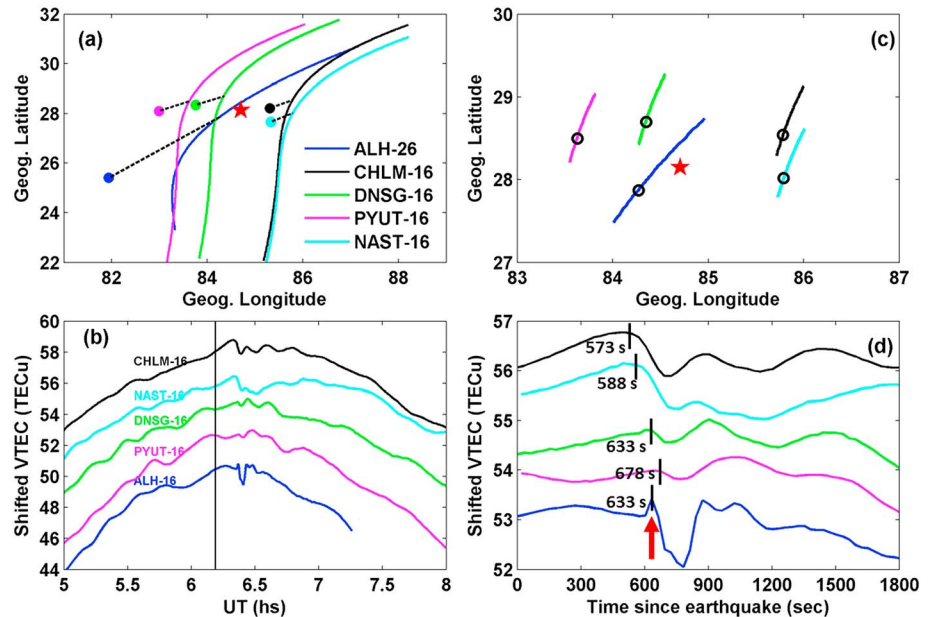

Figure 3. Travel time diagram of surface Rayleigh wave in the normalized vertical component of displacement from the BBS in east (a), south (b), and west (c) directions during the M_w 7.8 Gorkha, Nepal, earthquake on 25 April 2015 (see appendix for more details on the estimation of surface Rayleigh wave velocity).

Figure 4. The ionospheric VTEC perturbations observed in the vicinity of epicenter (within 150 km radius). (a) IPP tracks of GPS observations from the stations ALH, CHLM, NAST, DNSG, and PYUT (colored circles) during 05–08 UT along with the location of epicenter (red star). The dotted black lines joining the GPS stations and IPP tracks represent the ground projections of respective line-of-sight paths. (b) VTEC observations during 05–08 UT. Note VTEC observations from different stations are shifted by a constant offset in order to avoid the overlapping of curves for better visibility. (c and d) Same as Figures 4a and 4b with an enlarged scale for 30 min duration from the onset of earthquake. Black circles in Figure 4c represent the IPP locations of VTEC perturbations observed (shown) in Figure 4d (refer text for more details).

waves (Astafyeva et al., 2013; Zettergren et al., 2017), however, with a smaller amplitude and duration due to much smaller magnitude of Nepal earthquake (~M 7.8) compared to that of Tohoku-oki earthquake (~M 9.0).

The initial positive pulse that observed only in the southward direction (not observed in other directions) is further investigated in Figure 5. Figure 5a shows a set of nine IPP tracks (colored arcs) of GPS PRNs 16, 26, and 23 from the southern stations (ALH-16, NAGP-26, HYDE-26, ONGO-26, IISC-26, MBDR-23, DGPR-23, PORT-23, and HAVE-23). The colored solid circles indicate the locations of respective GPS stations. The black (thin) lines connecting the GPS stations and the corresponding IPP tracks indicate the ground projection of line-of-sight (LOS) path at the time of observed positive pulse in VTEC. The red star indicates the location of epicenter and triangles indicate the locations of six broadband seismometers (PBRI, DGPR, HYBD, BWNR, IITK, and BOKR) located south of the epicenter (see Table 1 for their coordinates). The VTEC from the above stations are shown in Figure 5b which are arranged in increasing order of epicentral distance by shifting with a constant offset to avoid the overlapping of the curves for better visibility. The initial positive pulse followed by the depletion in TEC can be observed from all the stations in the southward direction. Further, the positive pulse appears to be stretched and delayed in time as the distance increases from the epicenter (from ALH-16 to PORT-23). The arrival times of these positive pulses at different stations are indicated as black open circles in Figure 5b. Figure 5c shows the epicentral distances of positive pulses (black open circles) as a function of their arrival times at different locations from the onset of earthquake. The best fit straight line indicates that the apparent horizontal phase velocity of this positive pulse is 2.39 km/s (~2.4 km/s) which is substantially larger than the velocity of sound (or acoustic wave) in the upper atmosphere. The red triangles in Figure 5c represent the epicentral distances and arrival times of surface Rayleigh waves as observed from ground seismometers at six stations in the southward direction shown in Figure 5a (see appendix for identification of Rayleigh wave arrival times from seismometer data). The best fit straight line gives the propagation velocity of surface Rayleigh wave is ~3.7 km/s which is significantly higher than the propagation velocity of positive pulse. This suggest that this interesting positive pulse-like perturbation that observed only in southward direction propagated with a horizontal velocity of ~2.4 km/s which is substantially faster than acoustic velocity in the ionosphere and significantly slower than the surface Rayleigh wave; these will be discussed further in section 4.
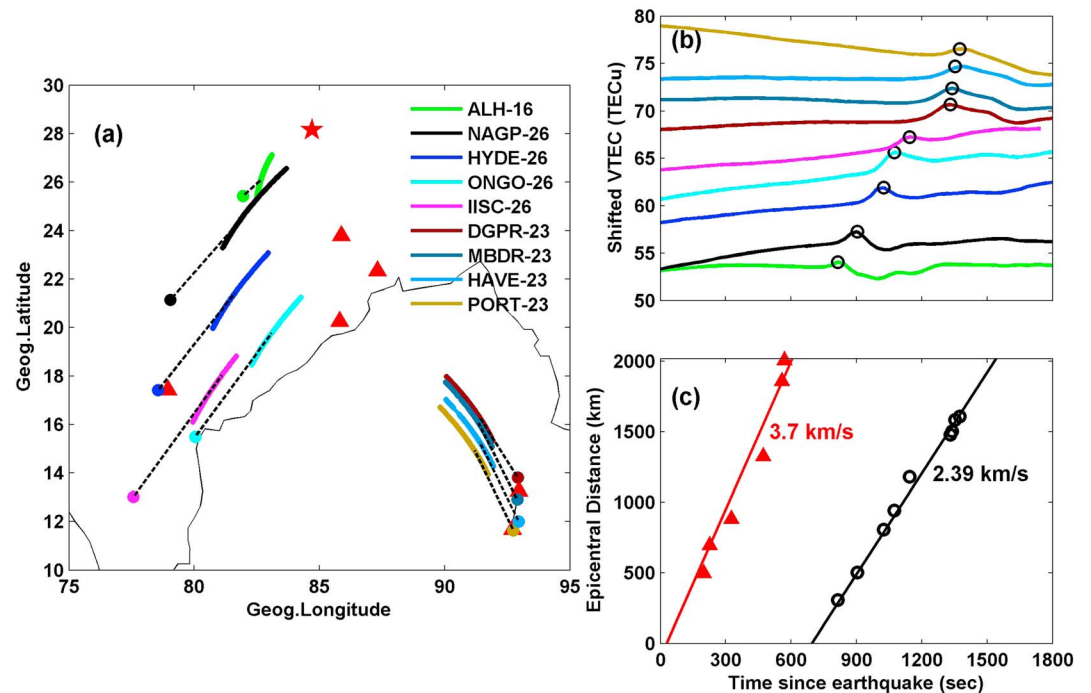
Figure 5. Ionospheric VTEC perturbations observed in south of epicenter from station-PRN pairs of ALH-16, NAGP-26, HYDE-26, ONGO-26, IISC-26, DGPR-23, MBDR-23, HAVE-23, and PORT-23. (a) The IPP tracks and the locations of ground-based GPS receivers (colored circles) and seismometers (red triangles) along with epicenter. The dotted black lines joining the GPS stations and IPP tracks represent the ground projections of respective line-of-sight paths. (b) VTEC observations for 30 min period from the onset of earthquake. Note VTEC observations from different stations are arranged with increasing epicentral distance by shifting with a constant offset in order to avoid the overlapping of curves for better visibility. The black open circles in Figure 5b indicate the arrival times of peak positive pulse observed from respective stations. (c) Epicentral distances of peak positive pulses (black open circles) as a function of their arrival times at different locations. The arrival times of surface Rayleigh wave measured by seismometers and their respective epicentral distances are also shown in red triangles (see appendix for more details on the estimation of surface Rayleigh wave velocity).

With a view to further investigate the coseismic traveling ionospheric disturbances (CTIDs), the GPS-VTEC observations from various stations are subjected to a band-pass filter with a passband of 1.5 to 10 mHz (~1.6 to 11 min) using a sixth-order Butterworth filter. In order to examine the directional properties of CTIDs, the filtered perturbations in VTEC are plotted as a function of azimuth angle with respect to earthquake epicenter as shown in Figure 6. Figure 6a shows the number of TEC observations as a function of azimuth angle. It can be seen from Figure 6a that the number of observations are sufficiently large at all azimuth angles except at small windows centered on ~40, 135, and 160°. Figure 6b shows the filtered VTEC perturbations as a function of azimuth angle. The filtered VTEC perturbations are further color modulated with the distance from the epicenter (epicentral distance) in Figure 6b. From Figure 6b, one can observe that the filtered VTEC perturbations found vary between ~−0.9 to 0.8 TEC units. The perturbations smaller than 0.05 TEC units can be considered as due to background noise. It is interesting to note that the larger VTEC perturbations (>0.2 or <−0.2 TEC units) are distributed between 25 and 225°. Also, the strong perturbations (>0.5 or <−0.5 TEC units) are mainly occurred between 60 and 225°, i.e., in the east and south directions. Further, it can be observed from this figure that the apparent VTEC perturbations are significantly smaller at azimuth angles greater than ~225° (i.e., west and north directions). The VTEC perturbation color modulated with the epicentral distances in Figure 6b indicates that the larger VTEC perturbations in east and south directions are distributed at both near and far distances. Similarly, the smaller VTEC perturbations in west and north directions are also distributed in the range of 40–1,500 km epicentral distance. This indicates that the smaller (larger) amplitude VTEC perturbations observed in west and north (east and south) directions are not influenced by their distances from the epicenter.

Further, the amplitudes of VTEC perturbations also depend on the viewing geometry between satellite and receiver, with respect to the seismic-induced wave fronts, because of phase cancellation effects along the
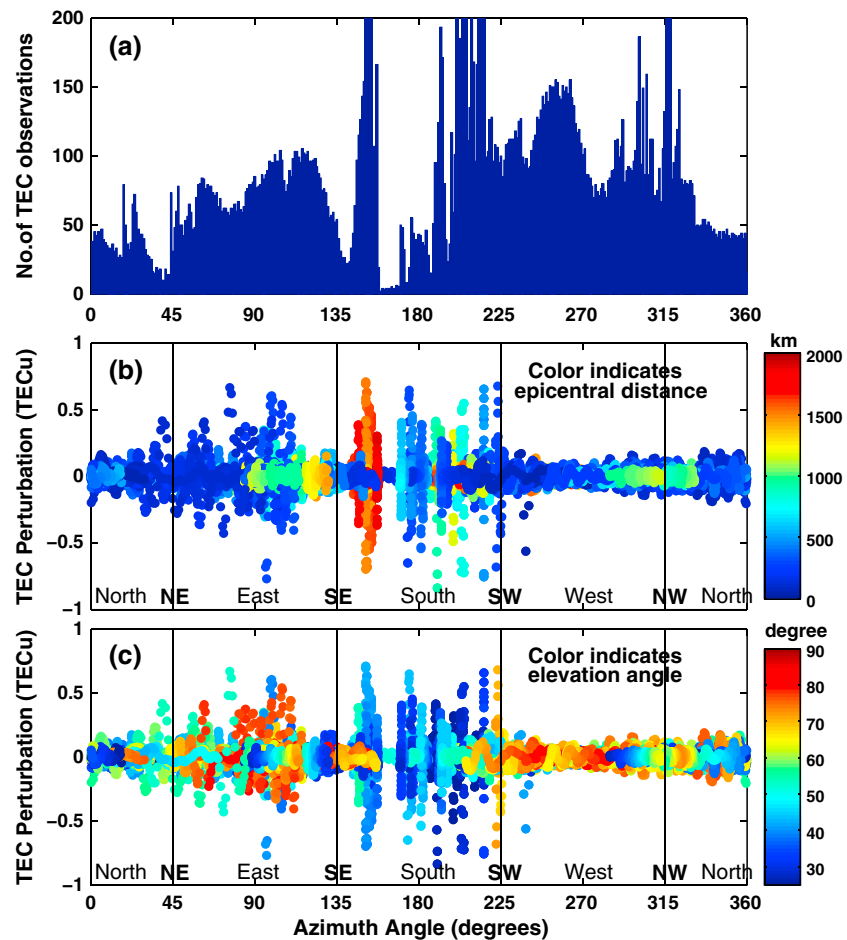
Figure 6. Azimuthal distribution of IPP locations of (a) VTEC observations and (b and c) filtered VTEC perturbations using a sixth-order Butterworth digital band-pass filter with a passband of 1.5 to 10 mHz (~1.6 to 11 min). The filtered VTEC perturbations are color modulated with the epicentral distances and elevation angles in Figures 6b and 6c, respectively.

integration (line-of-sight) path (Georges & Hooke, 1970Grawe & Makela, 2015). Hence, the observed azimuthal asymmetry in the amplitudes of VTEC perturbations can partly be influenced by the viewing geometry. In order to examine this, Figure 6c is plotted similar to that of Figure 6b except that the VTEC perturbations are color modulated with the elevation angles of GPS VTEC observations. It can be observed from Figure 6c that both larger amplitude perturbations (in south and east) and smaller amplitude perturbations (in west and north) are distributed nearly over the all range of elevation angles (i.e., ~25–85°). Therefore, from Figures 6b and 6c, the observed directivity of VTEC perturbations with larger amplitudes in east and south directions and smaller amplitudes in West and North directions are real and not fully influenced by the their epicentral distance and/or elevation angles.

The filtered VTEC perturbations are classified in to four groups based on the azimuthal angles of their IPP points with respect to epicenter as east (45°–135°), south (135°–225°), west (225°–315°), and north (315°–45°) as indicated in Figure 6. In Figure 7, the VTEC perturbations are plotted as a function of horizontal distance from the epicenter (epicentral distance). Figures 7a–7d show the travel time diagrams of CTIDs constructed from filtered VTEC perturbations in the east, south, west, and north directions, respectively. From Figure 7, one can observe the periodic wave-like oscillations with periods of 4–6 min in all the directions. The period of these oscillations appears to slightly increase at larger epicentral distances. The amplitudes of these oscillations are stronger on the south (Figure 7b) and east (Figure 7a) directions, relatively weaker in the north (Figure 7d) and significantly smaller in the west (Figure 7c) directions (note the difference in color scale between top and bottom panels). Further, the initial perturbation observed is a decrease in TEC in all directions except in the south. The TEC perturbation observed in the southward direction is initially positive
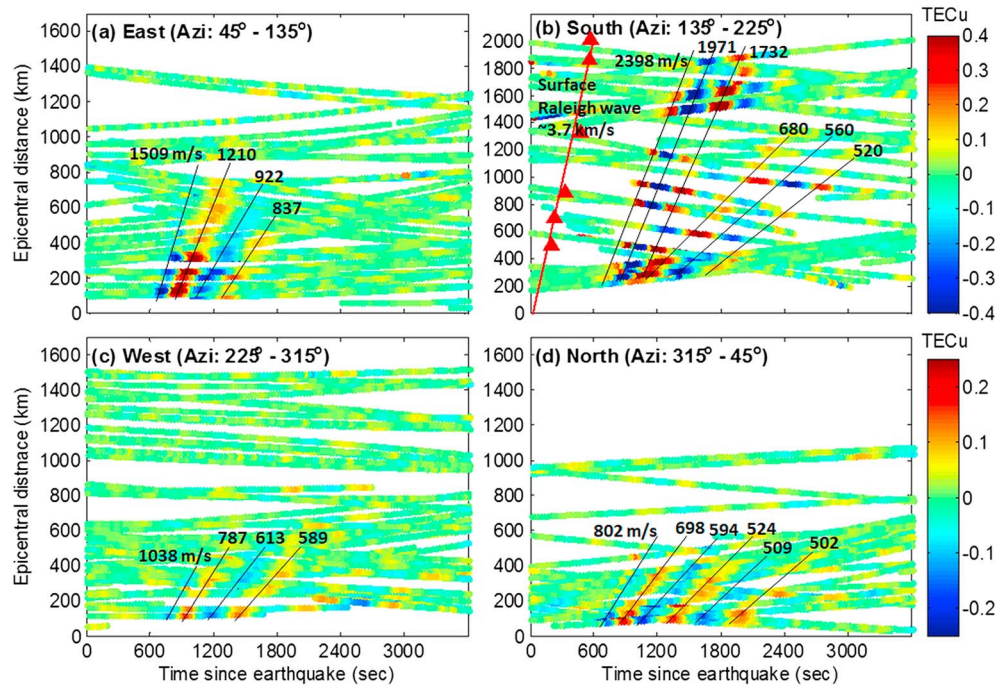
Figure 7. Travel time diagrams constructed from the band-pass filtered VTEC perturbations observations in (a) east, (b) south, (c) west, and (d) north directions. Note the difference in color scale between the top panels and bottom panels. The red triangles in Figure 7b represent the arrival times of surface Rayleigh waves at six southward BBS stations shown in Figure 5.

(Figure 7b) as shown earlier in Figure 5. The slopes of the best fit lines of TEC perturbations indicate the phase propagation velocity of CTIDs. The phase propagation velocity of initial positive perturbation in south (Figure 7b) is ~2392 m/s (~2.39 km/s). The velocities of subsequent negative and positive TEC perturbations are ~1.86 and 1.73 km/s. Further, it is an interesting note that the TEC perturbations in the southward direction (Figure 7b) appears to be split in to two modes: (i) fast mode perturbations with phase velocities varying from ~2.39–1.7 km/s and (ii) slow mode with velocities ranging from ~680 to 520 m/s (~0.68–0.52 km/s). This splitting of fast and slow propagating TEC perturbations can be clearly noticed from ~800 km epicentral distance and the splitting is not discernible in near field with distances less than ~800 km. Similar splitting of fast and slow mode propagating the TEC perturbations were first observed by Astafyeva et al. (2009) during Kuril earthquake at distances above ~900 km from the epicenter and also during Tohoku-oki earthquake (Liu et al., 2011; Rolland et al., 2011). They have attributed these fast and slow mode perturbations, most likely, to the acoustic waves triggered by the surface Rayleigh waves and earthquake shock, respectively. With the availability of surface Rayleigh wave information from the ground-based BBS, the arrival times of surface Rayleigh wave at the six southward BBS stations (shown in Figure 5) are plotted again in Figure 7b as red triangles for comparison. It can be noticed from Figure 7b (and Figure 5c) that the phase velocity of fast mode propagating TEC perturbations (~2.39–1.73 km/s) is relatively slower than the velocity of surface Rayleigh wave and will be discussed later. The splitting of fast and slow propagating CTIDs is not observed in other directions which could be due to lack of observations at farther distances and/or due to weaker amplitudes of TEC perturbations.

Further, it can be seen from the Figure 7 that the propagation velocities of CTIDs are not uniform in other directions. Though the fast mode CTIDs with velocities of (~2.4–1.7 km/s) were not observed in east, the velocity of initial negative TEC perturbation is 1509 ms^{-1} and the velocity of next positive perturbations is 1210 ms^{-1} which are higher than in other (north and west) directions. Further, it should be noted that the horizontal velocities of CTIDs in any direction are significantly smaller than the surface Rayleigh wave group velocities of ~3.4–3.7 km/s observed from ground-based seismometers (Figure 3). In other words, no clear Rayleigh wave imprint with a velocity of ~3.4–3.7 km/s has been observed in the ionospheric VTEC perturbations in any direction during this earthquake.
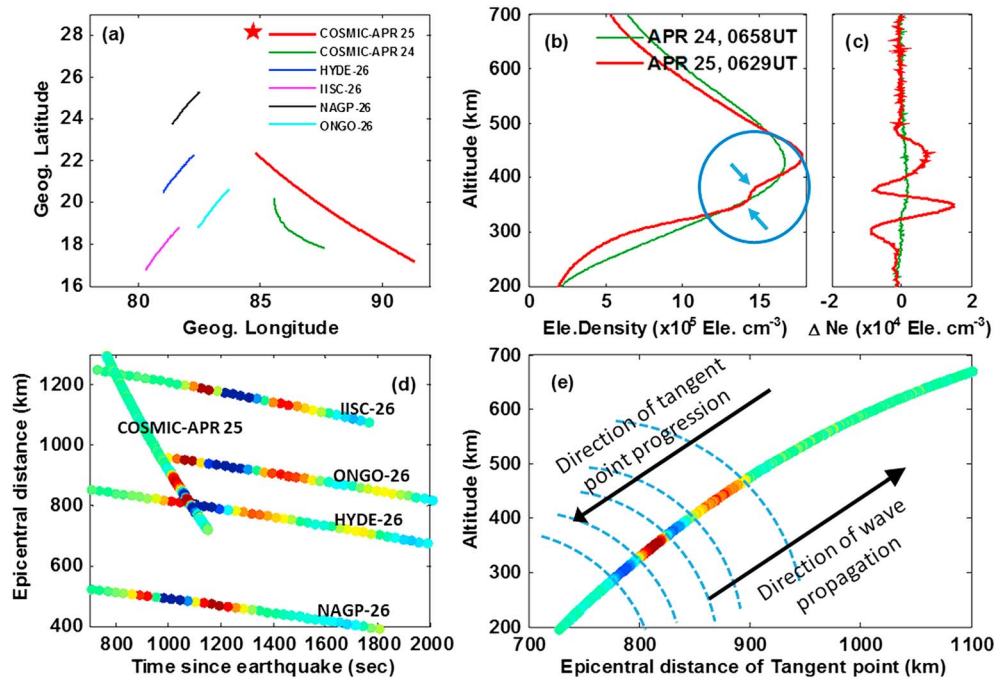
Figure 8. Simultaneous observations of ionospheric plasma density perturbations from ground-based GPS-VTEC and COSMIC radio occultation measurements. (a) IPP tracks of GPS from the four southward stations and tangent point projections of COSMIC RO observations. (b) Electron density perturbations observed in COSMIC radio occultation profile (red profile). The thin green profile also measured by COSMIC RO around the same location and UT from the same set of COSMIC-GPS satellite pair on previous day is shown for the comparison. (c) Detrended electron density perturbations from COSMIC RO profiles. (d) Filtered GPS-VTEC perturbations from four southward stations and detended electron density perturbations from RO profile as a function of time and epicentral distance (e) Detrended electron density perturbations as a function of epicentral distance on X axis and altitude on Y axis.

In Figure 8, we present the interesting observations from GPS radio occultation measurements from Formosat-3/COSMIC in comparison with the ground-based GPS-VTEC observations. Figure 8a shows the set of four IPP tracks of GPS PRN 26 from the southern stations NAGP-26, HYDE-26, ONGO-26, and IISC-26 (station locations, IPP tracks, and ground projections of LOS paths of the same can be observed from Figure 5a). Figure 8b shows the vertical electron density profile (red curve) measured from COSMIC radio occultation (RO) around 0622 UT on 25 April 2015. This is a setting occultation between COSMIC satellite (C-002) and GPS satellite (PRN-01) starting with the occultation (tangent) point altitude of 770 km at ~0622 UT and subsequently descending to 100 km at ~0630 UT. The occultation point location at top altitude (770 km) is 91.35°E, 17.17°N and at bottom altitude (100 km) is 85.15°E and 22.0°N. That means that the occultation point not only descends vertically from top to bottom but also sweeps horizontally a large distance (~841 km) from southeast to northwest direction. The ground projection of occultation point movement is shown as the red curve in Figure 8a. Another RO electron density profile measured from the same pair of COSMIC and GPS satellites (C-002 and PRN-01) around the same location at ~0658 UT on the previous day is also shown as a reference in Figure 8b (thin green curve). The occultation point track of this RO profile of the previous day is shown as thin green arc in Figure 8a.

The earthquake induced ionospheric plasma density perturbations can be observed form the RO profile around 300–500 km region as shown in Figure 8b. The F_2 layer peak electron density (N_mF_2) exhibits an enhancement compared with the previous day observation. However, the F_2 layer peak height (h_mF_2) is more or less similar to that of the previous day. The interesting feature that can be observed from Figure 8b is a cusp-like decrease in electron density around 375 km and an increase below the cusp around 350 km as indicated by the blue arrows. In order to clearly bring out these perturbations, a 20 km running mean is subtracted from the RO profile and the detrended perturbations are shown in Figure 8c. The detrended perturbations from the previous day profile were also shown in Figure 8c for comparison. One can observe a clear wave-like perturbation with two enhancements centered around 440 and 350 km, and depletions

around 375 and 300 km. Figure 8d shows the detrended electron density perturbations in RO profile as a function of time on X axis and epicentral distance on Y axis along with the band-pass filtered VTEC perturbations from the four GPS observations (shown in Figure 8a) for comparison. It can be clearly seen from the Figure 8d that both the epicentral distance and time of the initial positive perturbations in COSMIC RO profile and GPS VTEC observations nicely corresponds with each other. These results clearly indicate that the acoustic wave generated during to the earthquake has reached F_2 layer peak altitude and induced ionospheric plasma density perturbations around 300–440 km altitudes. It should be noted that similar detrending applied on the electron density profile around the same time and location on the previous day does not show any wave-like perturbations. This supports that the observed wave-like perturbations in Figure 8c are not an artifact and are indeed due to acoustic waves generated during the earthquake. However, the electron density perturbations in COSMIC RO profile appear to be of shorter duration than in the VTEC perturbations. The shorter wavelengths of electron density perturbations in RO profile are mainly due to rapid progression of tangent point (~1.7 km/s) in the opposite direction to the southward propagating CTIDs (~2.4–1.7 km/s). For example, Figure 8e shows the detrended electron density perturbations as a function of epicentral distance (X axis) and tangent point altitude (Y axis). The directions of tangent point progression and the southward propagating CTIDs are as indicated in Figure 8e. It should be noted here that the COSMIC RO profile is derived from line of sight TEC measurements between COSMIC (C002) and GPS (PRN01) satellites and using Abel retrieval method (Lei, Syndergaard, & Burns, 2007; Tulasi Ram et al., 2015). The viewing (line-of-sight) geometry between the COSMIC and GPS satellites and the progression of tangent point through the CTIDs would significantly influence the amplitudes and wavelengths of electron density perturbations in RO observation. Hence, it can be expected that the amplitudes and wavelengths in RO electron density and GPS TEC perturbations are not quantitatively comparable. Nevertheless, the correspondence in time and epicentral distance of wave-like perturbations in RO profile and GPS TEC observations shown in Figure 8d justifies that the perturbations in the RO profile are due to southward propagating CTIDs. Sun et al. (2016) have also shown that the observed perturbations in this electron density profile are due to the earthquake by estimating time and location of perturbation, and the velocity of acoustic wave generated by the earthquake. However, they interpreted the observed perturbation at F_2 layer peak region as due to the uplift of h_mF_2 by 34.4 km within 0.5 to 1 min which corresponds to a very large vertical velocity of 573–1,147 m/s. However, we argue that the induced perturbations at F_2 layer peak region are not due to the rapid uplift of h_mF_2. Instead, the observed positive and negative perturbations in electron density are mainly due to the passage of occultation point through the positive and negative phases of coseismic traveling ionospheric disturbance which is propagating outward from the epicenter as shown in Figure 8e.

4. Discussion

The sudden coseismic upward displacement of Earth surface during the earthquakes excites acoustic waves into the atmosphere. As the atmospheric density decreases exponentially with altitude, the amplitudes of the induced waves increase exponentially with height because of the conservation of energy. The amplitudes of these atmospheric acoustic waves will be amplified by ~10^5–10^6 times at the ionospheric altitudes with respect to the ground level. These waves interact with ionospheric plasma via ion-neutral collisions and can cause similar perturbations in ionospheric electron content. While the atmospheric acoustic waves propagating upward, the velocity of upward propagation varies with altitude which primarily depends on the neutral temperature. The delay of ~9–11 min for the initial perturbation in ionospheric VTEC (Figure 4) is well consistent with the time taken by the acoustic wave to reach the ionospheric F region altitudes (250–300 km) considering the velocity of sound in atmospheric layers. The compression (steepening) and rarefaction type oscillation in the acoustic wave is ascribed to induce an "N-type" perturbation with initial positive and followed by depletion in VTEC (Astafyeva & Heki, 2009; Astafyeva et al., 2013; Rolland et al., 2011; Zettergren et al., 2017). Saito et al. (2011) have also reported an N-type perturbation with a sharp enhancement followed by a long depletion in TEC during Tohoku-oki earthquake in Japan on March 11, 2011. However, in the present case, such an N-type perturbation with initial positive phase is observed only in the southward direction (Figures 5). While in other directions, only the depletion in VTEC without the prior positive phase is observed (Figures 4, 5, and 7). As the acoustic waves propagate vertically, the corresponding velocities can significantly increase due to the exponential decay of background atmospheric density and resultant nonlinear effects

leads to the formation of shock front (Astafyeva et al., 2013; Zettergren et al., 2017). The shock front ahead of the wave pushes the plasma upward (Astafyeva et al., 2011). However, because of the highly geomagnetic field aligned nature of plasma, the ionized gas tends to move along the geomagnetic field lines toward south due to the inclination of field lines. This plasma transport along the field lines toward south by the shock front can result in a positive initial VTEC perturbation in southward direction. Rolland et al. (2013) have also reported that the initial positive phase of N-type perturbation is observed only on the south of the epicenter during the inland Van earthquake (on 23 October 2011) in Eastern Turkey which is explained in terms of geomagnetic field effect. Later, Zettergren et al. (2017), through model simulations for undersea earthquake disturbances, have successfully shown the formation of positive TEC perturbation due to shock front only in the southward (equatorward) direction. The steep shock front also causes rapid upward transport of neutral gas, which eventually begins to fall as the atmosphere recovers; the net impact of the nonlinear acoustic wave dissipation in the thermosphere gives rise to a downward field-aligned flow of the ionosphere. This can result in enhanced plasma recombination and depletion in VTEC in all directions near the epicenter (Astafyeva et al., 2013; Zettergren et al., 2017).

The initial positive phase observed in south of epicenter is further found to propagate with a supersonic velocity of ~2.39 km/s. This velocity of ~2.39 km/s observed in Figure 5 is consistent with the reported velocities of 2.4 and 2.6 km/s by Reddy and Seemala (2015) and Catherine et al. (2016), respectively, for VTEC perturbations which they have attributed to Rayleigh wave. Further, Chen et al., (2017) have shown that the Rayleigh wave-induced perturbations in VTEC is ~1.6 km/s in the near field of 0–500 km epicentral distance, which is further increased to 2.35 km/s at 500–1,500 km and 2.74 km/s at 1,500–4,000 km in the far field. However, these reported velocities are significantly smaller than the surface Rayleigh wave group velocity of ~3.4–3.7 km/s observed from the ground-based seismometers. This suggest that the Rayleigh wave imprint in the ionosphere with the same velocity as the surface Rayleigh wave at ground is not observed during this earthquake. Jin et al. (2017) have also compared the CTIDs with the surface vertical displacements using ground-based seismometers and bottom pressure records during the Haida Gwaii earthquake in Canada on 28 October 2012. They have found that the apparent horizontal phase velocity of CTIDs (~2.20 km/s) is significantly slower than the surface Rayleigh waves on ground (~4.05 km/s), but consistent with sea bottom pressure disturbances (~2.2 km/s) during Haida Gwaii earthquake. The unsuccessful detections of surface Rayleigh wave imprint in the ionosphere could be due to the superposition of acoustic waves generated by the main shock (shock acoustic wave) of the earthquake and the acoustic waves continuously excited by the propagating surface Rayleigh wave in the near field close to the epicenter. Kakinami et al. (2013) have proposed that a superimposed acoustic wave front can be formed by the continuously excited acoustic waves due to propagating surface Rayleigh wave. The oscillation of this superimposed wave front is nearly parallel along the field lines in the southward direction and hence can induce significant ionospheric VTEC perturbations in the south of the epicenter. Therefore, we interpret that the observed positive VTEC perturbation with a velocity of ~2.4 km/s in the southward direction (Figures 5 and 7b) is not a true Rayleigh wave imprint, instead could due to the superimposed acoustic wave front with an apparent slower velocity than that of surface Rayleigh wave at ground due to the mixture of shock acoustic waves and acoustic waves excited by the propagating Rayleigh wave. Dučić et al. (2003) have observed southward CTIDs with a velocity similar to that of surface Rayleigh wave (3.48 km/s) during the 2002 Denali earthquake. However, the Rayleigh wave imprint in the ionosphere is not clear in the near field and becomes detectable at ~3,000 km of epicentral distance (see Figure 2 of Dučić et al., 2003). During the Kuril earthquake in 1994, Astafyeva et al. (2009) have also shown that the CTIDs propagate with an apparent velocity slower than the Rayleigh wave in the near field; which later separates into "fast" and "slow" components at distances ~900 km from the epicenter due to the differences in the characteristic velocities of Rayleigh wave and shock acoustic wave. Similar, splitting of fast (~2.4–1.7 km/s) and slow (680–520 m/s) propagating CTIDs has been observed in southward direction at ~800 km epicentral distance. However, in the present study, the phase velocity of fast mode CTIDs is relatively slower than the velocity of surface Rayleigh wave estimated from the ground-based BBS (~3.7 km/s). Therefore, the CTIDs with supersonic velocities in the southward direction (Figures 5 and 7b), but slower than the surface Rayleigh wave, can be interpreted as due to superimposed wave front formed by the blend of shock acoustic waves by the sudden coseismic thrusting and continuously excited acoustic waves by the propagating Rayleigh wave.
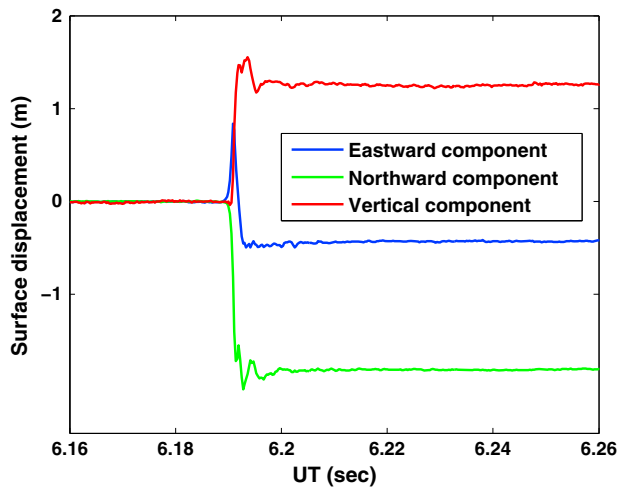
Figure 9. The eastward (blue), northward (green), and vertical (red) components of surface displacement during the main shock of the earthquake measured by high rate (1 s) ground-based GPS receiver at a station KKN4 (85.28°E, 27.80°N) very close to the region of maximum surface deformation occurred during the Gorkha, Nepal, earthquake (see Figure 1).

Further, the amplitudes and phase propagation velocities of induced CTIDs are significantly larger in both south and east directions (Figure 7). The enhanced amplitudes of VTEC perturbations in the southward direction can partly be due to the geomagnetic field effect. As the plasma tends to move freely along the field lines, the coupling between the acoustic waves and plasma maximizes in the direction parallel to the geomagnetic field lines (Rolland et al., 2013). For the earthquakes occurred in Northern Hemisphere, the radially outward acoustic waves propagate parallel to the field lines toward south and across the field lines toward north. As a result, the ionosphere is more effectively perturbed; hence, larger VTEC perturbations can be observed in the southward direction. In addition to the geomagnetic field effect, the directivity of induced acoustic wave field during the earthquake can also significantly influence the directivity of induced TEC perturbations. Indeed, the observed east-west asymmetry in the VTEC perturbations indicates the role of source (acoustic wave) field radiation characteristics. Sunil et al. (2017) also reported the correlation of the coseismic ionospheric perturbations and rupture propagation during the Gorkha earthquake. Further, the crustal deformation during the earthquake also shows a large southward and eastward (southeastward) movement of earth surface. For example, Figure 9 shows the surface displacement measured from the ground-based GPS observations at high (1 s) sampling rate at a station KKN4 (85.28°E, 27.80°N) very close to the region of maximum uplift occurred during this earthquake (see Figure 1). The blue, green, and red curves represent the eastward, northward, and vertical components of surface displacement, respectively. It can be observed from this figure that the surface displacement exhibits initially an impulsive eastward movement of 0.8 m (blue curve) and a large southward movement of 1.8 m (green) along with the vertical displacement of 1.4 m (red curve) during the main shock of the earthquake. Hence, it can be expected that the main emission lobe of energy is directed toward southeast due to impulsive southeastward surface displacement in the uplifted region. In other words, the larger amplitudes of acoustic waves generated in southeast direction due to the combination of rupture propagation direction and the associated surface deformation during the main shock of quake which would cause large VTEC perturbations in the southeast directions. The larger amplitudes and faster phase propagation velocities of VTEC perturbations in south and east directions (Figures 7b and 7a) consistent with this argument. Courboulex et al. (2013) have shown that the seismic waves during the large earthquakes exhibit larger amplitudes in the rupture propagation and thrust direction. Further, Zettergren and Snively (2015) have shown through model simulations that more directive acoustic wave fields produce TEC perturbations with apparent horizontal phase speeds above the sound speed. During this Nepal earthquake, the piston-like uplift of surface occurred with a large southward (~1.8 m) and eastward (~0.8 m) displacements (Figure 9) and rupture is mainly propagated toward southeast direction as shown in Figure 1. Hence, the larger amplitudes and faster propagation velocities of CTIDs observed in south and east could probably attributed to the large amplitude acoustic wave fields directed toward southeast due to the nature of crustal deformation and the rupture propagation during this earthquake, in addition to the geomagnetic field effect. Needless to say, this hypothesis needs to be further validated using model simulations.

Finally, the vertical electron density profile from COSMIC radio occultation observations has captured the induced ion density perturbations around 300 to 440 km altitudes. Sun et al. (2016) have attributed the observed changes in RO profile to rapid uplift of F_2 layer peak altitude. On the contrary, we have shown that the observed ion density perturbations in the RO profile are mainly due to the horizontal progression of occultation (tangent) point through the positive and negative phases of southward propagating CTID as demonstrated in Figure 8. Thus, no specific observation of uplifting h_mF_2 is noted as compared to the RO profile taken around the same location and time on the previous day. Further, our analysis and interpretation can explain the cusp-like decrease in the electron density below h_mF_2 (around 375 km, Figure 8b) and wave-like variation observed in the detrended profile (Figure 8c) as due to progression of occultation point through the southward CTIDs, whereas this cusp-like decrease in the profile was not discussed in the report of Sun et al. (2016).

5. Summary and Conclusions

A detailed investigation on the CTIDs and their relationship with the nature of crustal deformation and surface Rayleigh waves has been carried out using a set of ground-based GPS receivers and seismometers along with COSMIC radio occultation observations during the Gorkha, Nepal, earthquake on 25 April 2015. The important findings are briefly summarized hereunder. The vertical displacement observations from the ground-based seismometers show that the surface Rayleigh waves propagated in all directions with a group velocity of ~3.4–3.7 km/s. The initial ionospheric perturbation is detected as depletion in VTEC (ionospheric hole) above the epicenter about 9–11 min after the earthquake onset. This ionospheric hole is preceded by a positive phase, similar to N-type perturbation, on the south due to the steepening by the shock front directed parallel to the geomagnetic field lines. The CTIDs with periods of ~4 to 6 min were observed to propagate in all directions, however, with significantly larger amplitudes and faster apparent phase velocities in south and east directions, which are attributed to the radiation pattern of acoustic wave field due to coseismic surface thrusting in addition to the geomagnetic field effect. The southward CTIDs were further found to split in to fast (~2.4–1.7 km/s) and slow (680–520 m/s) modes at distances greater than ~800 km from the epicenter. The velocity of fast mode southward CTID (~2.4 km/s) is substantially faster than the velocity of sound in thermosphere, however, significantly smaller than the group velocity of surface Rayleigh wave observed from seismometers on ground. This suggest that the observed supersonic velocity of southward propagating wave is not the true surface Rayleigh wave imprint in the ionosphere; instead it can be attributed to the superimposed wave front formed by the superposition of shock acoustic waves and continuously excited acoustic waves due to propagating Rayleigh wave. The vertical electron density profile from the COSMIC RO observation has captured the southward CTIDs and provides direct evidence for the propagation of CTIDs at F_2 region peak altitudes of ~300–440 km.

Appendix A: Rayleigh Wave Velocity

The analysis of vertical displacement data from broadband seismometer (BBS) observations and the method of identification of Rayleigh wave arrival times considered in this study are described here. As mentioned in the manuscript text, the BBS data collected under Indian seismic network by various agencies under Earth System Sciences Organizations were not calibrated to common amplitude scale. Therefore, we have
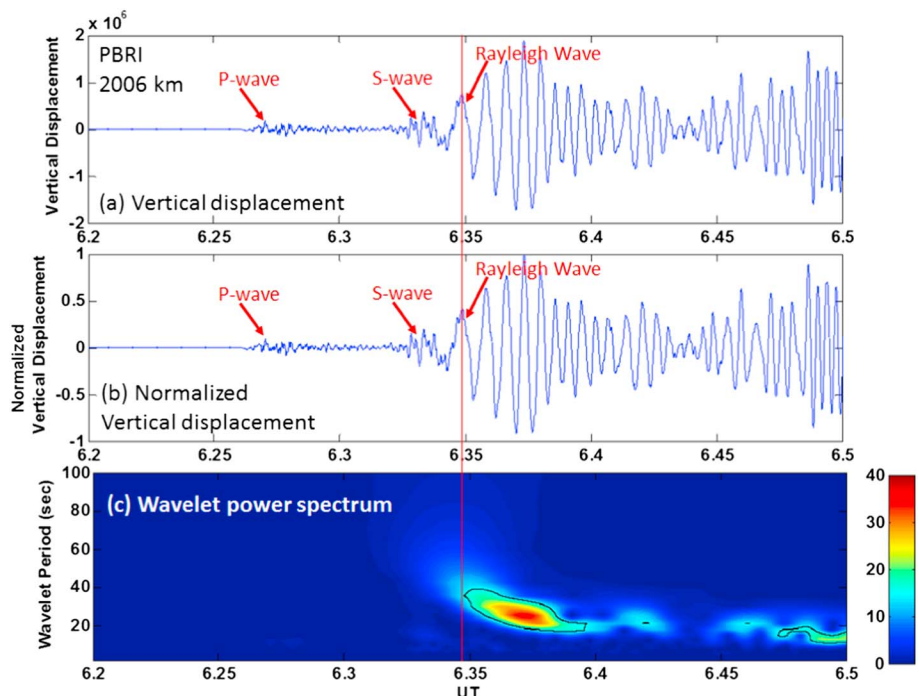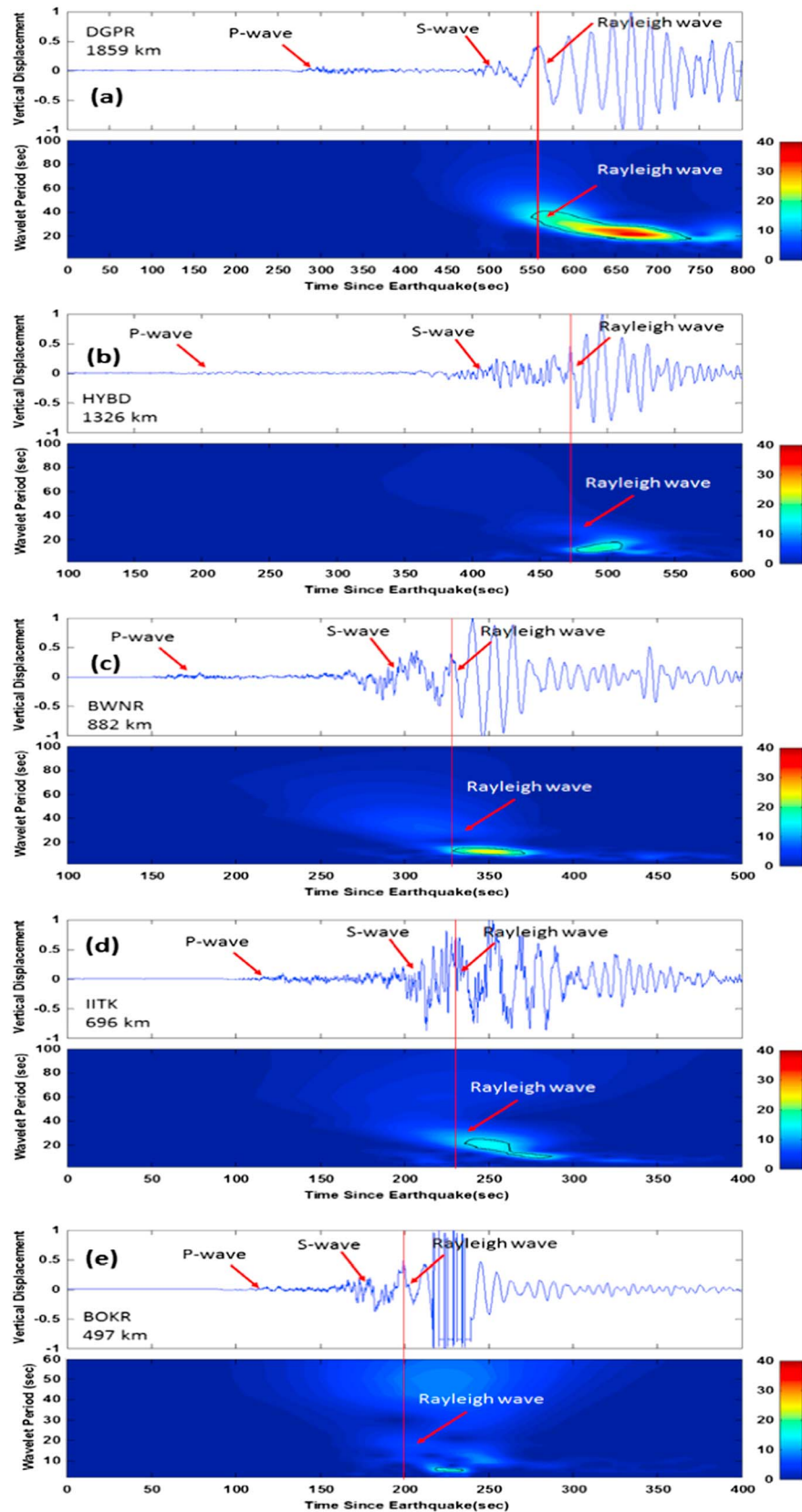

Figure A1. (a) Vertical displacement and (b) normalized vertical displacement and (c) wavelet spectrum of vertical displacement from BBS observations at Port Blair (PBRI).

Figure A2. The normalized vertical displacement and absolute wavelet power spectra of normalized vertical displacement from BBS observations at (a) DGPR, (b) HYBD, (c) BWNR, (d) IITK, and (e) BOKR.

normalized the waveform data by the maximum amplitude of vertical displacement between 06 and 07 UT. For example, below Figure (A1) shows the vertical displacement component data from the BBS at Port Blair (*PBRI*) that is ~2,006 km away from the epicenter. Figure A1a represents the original waveform data of vertical displacement (units not mentioned as they are not calibrated), and Figure A1b shows normalized waveform data of vertical displacement (normalized by the maximum amplitude between 06 and 07 UT). The arrival of Primary wave (*P* wave), Shear wave or secondary wave (*S* wave), and surface Rayleigh wave can be identified as marked in the figure. The body waves (primary and secondary waves) arrive earlier because of their high traveling velocities. The surface Rayleigh wave appears later because of the relatively slower velocity than the body waves. The Rayleigh waves travel along the surface of the Earth, and the particle motion of Rayleigh wave is larger than that of body waves; thus, they tend to cause more vertical displacement and damage. After the arrival of *P* wave and *S* wave, the arrival of surface Rayleigh waves can be identified by their large amplitudes in vertical displacement in seismometer data. In the present study, the peak of the first ripple with relatively large amplitudes than the *P* and *S* waves is considered as the time of arrival of Rayleigh wave as shown in the Figures A1a and A1b.

With a view to further examine the spectral characteristics of wave form data, the normalized vertical displacement data is subjected to wavelet analysis. Figure A1c shows the corresponding wavelet power spectrum. It can be seen from this figure that the absolute wavelet power enhances significantly with the arrival of large amplitude surface Rayleigh waves. The absolute wavelet power corresponds to ~15 units (black contour in bottom panel) at the time of arrival of Rayleigh wave at 570 s (~6.35 UT) from the earthquake onset (red vertical line). Therefore, in the present study, we are tracing the two features for the identification of the arrival time of surface Rayleigh waves as (i) the peak of the first ripple with relatively large amplitude than *P* and *S* waves in vertical displacement and (ii) the peak of the ripple that corresponds in time with approximately 15 units in absolute wavelet power as shown in the Figure A1.

Figure A2 shows the normalized vertical displacement and absolute wavelet power spectra from the other five southward stations, *DGPR*, *HYBD*, *BWNR*, *IITK*, and *BOKR* which are approximately 1859 km, 1326 km, 882 km, 696 km, and 497 km from the epicenter, respectively. The body waves (*P* and *S* waves) and the arrival of surface Rayleigh waves are marked in the figure. The arrival times of Rayleigh waves at DGPR, HYBD, BWNR, IITK, and BOKR are identified as 558 s, 473 s, 327 s, 228 s and 200 s from the onset of earthquake by tracing the amplitude and spectral features mentioned above. The vertical displacement data at the BOKR (a station relatively closer to the epicenter) is saturated due to large amplitude of Rayleigh waves higher than the dynamic range of the seismometer (Figure A2e). Hence, the wavelet power spectrum from BOKR data is ambiguous. Thus, only the amplitude feature is considered to identify the arrival time of Rayleigh wave at this station. Finally, the group velocity of surface Rayleigh wave in the southward direction is computed from the arrival times at the respective stations (epicentral distances) using the linear least squares fit as shown in the Figures 5c and 7b.

References

Acton, C. E., Priestley, K., Gaur, V. K., & Rai, S. S. (2010). Group velocity tomography of the indo-Eurasian collision zone. *Journal of Geophysical Research*, *115*, B12335. https://doi.org/10.1029/2009JB007021

Astafyeva, E., & Heki, K. (2009). Dependence of waveform of near-field coseismic ionospheric disturbances on focal mechanisms. *Earth, Planets and Space*, *16*, 939–943.

Astafyeva, E., Heki, K., Kiryushkin, V., Afraimovich, E. L., & Shalimov, S. (2009). Two-mode long-distance propagation of coseismic ionosphere disturbances. *Journal of Geophysical Research*, *114*, A10307. https://doi.org/10.1029/2008JA013853

Astafyeva, E., Lognonné, P., & Rolland, L. (2011). First ionospheric images of the seismic fault slip on the example of the Tohoku-oki earthquake. *Geophysical Research Letters*, *38*, L22104. https://doi.org/10.1029/2011GL049623

Astafyeva, E., Shalimov, S., Olshanskaya, E., & Lognonné, P. (2013). Ionospheric response to earthquakes of different magnitudes: Larger quakes perturb the ionosphere stronger and longer. *Geophysical Research Letters*, *40*(9), 1675–1681. https://doi.org/10.1002/grl.50398

Calais, E., & Minster, J. B. (1995). GPS detection of ionospheric perturbations following the January 17, 1994, Northridge earthquake. *Geophysical Research Letters*, *22*(9), 1045–1048. https://doi.org/10.1029/95GL00168

Catherine, J. K., Uma Maheshwari, D., Gahalaut, V. K., Roy, P. N. S., Khan, P. K., & Puviarasan, N. (2016). Ionospheric disturbances triggered by the 25 April, 2015 M7.8 Gorkha earthquake, Nepal: Constraints from GPS TEC measurements. *Journal of Asian Earth Sciences*, *133*, 80–88. https://doi.org/10.1016/j.jseaes.2016.07.014

Chen, P., Yao, Y., & Yao, W. (2017). On the coseismic ionospheric disturbances after the Nepal Mw7.8 earthquake on April 25, 2015 using GNSS observations. *Advances in Space Research*, *59*(1), 103–113. https://doi.org/10.1016/j.asr.2016.09.021

Coisson, P., Lognonne, P., Walwer, D., & Rolland, L. M. (2015). First tsunami gravity wave detection in ionospheric radio occultation data. *Earth and Space Science*, *2*(5), 125–133. https://doi.org/10.1002/2014EA000054

Courboulex, F., Dujardin, A., Vallée, M., Delouis, B., Sira, C., Deschamps, A., … Thouvenot, F. (2013). High-frequency directivity effect for an Mw 4.1 earthquake, widely felt by the population in southeastern France. *Bulletin of the Seismological Society of America*, *103*(6), 3347–3353. https://doi.org/10.1785/0120130073

Dučić, V., Artru, J., & Lognonné, P. (2003). Ionospheric remote sensing of the Denali earthquake Rayleigh surface waves. *Geophysical Research Letters*, *30*(18), 1951. https://doi.org/10.1029/2003GL017812

Georges, T. M., & Hooke, W. H. (1970). Wave-induced fluctuations in ionospheric electron content: A model indicating some observational biases. *Journal of Geophysical Research*, *75*(31), 6295–6308. https://doi.org/10.1029/JA075i031p06295

Grawe, M. A., & Makela, J. J. (2015). The ionospheric responses to the 2011 Tohoku, 2012 Haida Gwaii, and 2010 Chile tsunamis: Effects of tsunami orientation and observation geometry. *Earth and Space Science*, *2*(11), 472–483. https://doi.org/10.1002/2015EA000132

Heki, K., & Ping, J.-S. (2005). Directivity and apparent velocity of the coseismic ionospheric disturbances observed with a dense GPS array. *Earth and Planetary Science Letters*, *236*(3-4), 845–855. https://doi.org/10.1016/j.epsl.2005.06.010

Jin, S., Jin, R., & Li, D. (2017). GPS detection of ionospheric Rayleigh wave and its source following the 2012 Haida Gwaii earthquake. *Journal of Geophysical Research: Space Physics*, *122*(1), 1360–1372. https://doi.org/10.1002/2016JA023727

Kakinami, Y., Kamogawa, M., Tanioka, Y., Watanabe, S., Gusman, A. R., Liu, J.-Y., … Mogi, T. (2012). Tsunamigenic ionospheric hole. *Geophysical Research Letters*, *39*, L00G27. https://doi.org/10.1029/2011GL050159

Kakinami, Y., Kamogawa, M., Watanabe, S., Odaka, M., Mogi, T., Liu, J.-Y., … Yamada, T. (2013). Ionospheric ripples excited by superimposed wave fronts associated with Rayleigh waves in the thermosphere. *Journal of Geophysical Research: Space Physics*, *118*(2), 905–911. https://doi.org/10.1002/jgra.50099

Kamogawa, M., Kanaya, T., Orihara, Y., Toyoda, A., Suzuki, Y., Togo, S., & Liu, J.-Y. (2015). Does an ionospheric hole appear after an inland earthquake? *Journal of Geophysical Research*, *120*(11), 9998–10,005. https://doi.org/10.1002/2015JA021476

Kobayashi, H., Koketsu, K., Miyake, H., Takai, N., Shigefuji, M., Bhattari, M., & Sapkota, S. N. (2016). Joint inversion of teleseismic, geodetic, and near-field waveform datasets for rupture process of the 2015 Gorkha, Nepal, earthquake. *Earth, Planets and Space*, *68*(1), 66. https://doi.org/10.1186/s40623-016-0441-1

Koketsu, K., Miyake, H., Guo, Y., Kobayashi, H., Masuda, T., Davuluri, S., … Sapkota, S. N. (2016). Widespread ground motion distribution caused by rupture directivity during the 2015 Gorkha, Nepal earthquake. *Scienctific Reports*, *6*(1), 28,536. https://doi.org/10.1038/srep28536

Lei, J., Syndergaard, S., & Burns, A. G. (2007). Comparison of COSMIC ionospheric measurements with ground-based observations and model predictions: Preliminary results. *Journal of Geophysical Research*, *112*, A07308. https://doi.org/10.1029/2006JA012240

Lindsey, E., Natsuaki, R., Xu, X., Shimada, M., Hashimoto, H., Melgar, D., & Sandwell, D. (2015). Line of sight deformation from ALOS-2 inter-ferometry: M_w 7.8 Gorkha earthquake and M_w 7.3 aftershock. *Geophysical Research Letters*, *42*(16), 6655–6661. https://doi.org/10.1002/2015GL065385

Liu, J. Y., Tsai, Y. B., Chen, S. W., Lee, C. P., Chen, Y. C., Yen, H. Y., … Liu, C. (2006). Giant ionospheric disturbances excited by the M9.3 Sumatra earthquake of 26 December 2004. *Geophysical Research Letters*, *33*, L02103. https://doi.org/10.1029/2005GL023963

Liu, J.-Y., Chen, C.-H., Lin, C.-H., Tsai, H.-F., Chen, C.-H., & Kamogawa, M. (2011). Ionospheric disturbances triggered by the 11 March 2011 *M*9.0 Tohoku earthquake. *Journal of Geophysical Research*, *116*, A06319. https://doi.org/10.1029/2011JA016761

Mannucci, A. J., Wilson, B. D., & Edwards, C. D. (1993). A new method for monitoring the earth's ionospheric total electron content using the GPS global network. In: Proceedings of ION GPS-93. (pp. 1323–1332). Institute of Navigation.

Otsuka, Y., Kotake, N., Tsugawa, T., Shiokawa, K., Ogawa, T., Effendy, S., … Komolmis, T. (2006). GPS detection of total electron content variations over Indonesia and Thailand following the 26 December 2004 earthquake. *Earth, Planets and Space*, *58*(2), 159–165. https://doi.org/10.1186/BF03353373

Rama Rao, P. V. S., Gopi Krishna, S., Niranjan, K., & Prasad, D. S. V. V. D. (2006). Study of spatial and temporal characteristics of L-band scintillations over the Indian low-latitude region and their possible effects on GPS navigation. *Annales Geophysicae*, *24*(6), 1567–1580. https://doi.org/10.5194/angeo-24-1567-2006

Reddy, C. D., & Seemala, G. K. (2015). Two-mode ionospheric response and Rayleigh wave group velocity distribution reckoned from GPS measurement following M_w 7.8 Nepal earthquake on 25 April 2015. *Journal of Geophysical Research: Space Physics*, *120*(8), 7049–7059. https://doi.org/10.1002/2015JA021502

Rolland, L., Lognonne, P., Astafyeva, E., Kherani, A., Kobayashi, N., Mann, M., & Munekane, H. (2011). The resonant response of the ionosphere imaged after the 2011 off the Pacific coast of Tohoku earthquake. *Earth, Planets and Space*, *63*(7), 853–857. https://doi.org/10.5047/eps.2011.06.020

Rolland, L. M., Vergnolle, M., Nocquet, J.-M., Sladen, A., Dessa, J.-X., Tavakoli, F., … Cappa, F. (2013). Discriminating the tectonic and non-tectonic contributions in the ionospheric signature of the 2011, M_w7.1, dip-slip Van earthquake, Eastern Turkey. *Geophysical Research Letters*, *40*(11), 2518–2522. https://doi.org/10.1002/grl.50544

Saito, A., Tsugawa, T., Otsuka, Y., Nishioka, M., Iyemori, T., Matsumura, M., … Choosakul, N. (2011). Acoustic resonance and plasma depletion detected by GPS total electron content observation after the 2011 off the Pacific coast of Tohoku earthquake. *Earth, Planets and Space*, *63*(7), 863–867. https://doi.org/10.5047/eps.2011.06.034

Seemala, G. K., & Valladares, C. E. (2011). Statistics of total electron content depletions observed over the south American continent for the year 2008. *Radio Science*, *46*, RS5019. DOI: https://doi.org/10.1029/2011RS004722

Sreejith, K. M., Sunil, P. S., Agrawal, R., Saji, A. P., Ramesh, D. S., & Rajawat, A. S. (2016). Coseismic and early postseismic deformation due to the 25 April 2015, M_w 7.8 Gorkha, Nepal, earthquake from InSAR and GPS measurements. *Geophysical Research Letters*, *43*(7), 3160–3168. https://doi.org/10.1002/2016GL067907

Sun, Y.-Y., Liu, J.-Y., Lin, C.-Y., Tsai, H.-F., Chang, L. C., Chen, C.-Y., & Chen, C.-H. (2016). Ionospheric F_2 region perturbed by the 25 April 2015 Nepal earthquake. *Journal of Geophysical Research: Space Physics*, *121*(6), 5778–5784. https://doi.org/10.1002/2015JA022280

Sunil, A. S., Bagiya, M. S., Catherine, J., Rolland, L., Sharma, N., Sunil, P. S., & Ramesh, D. S. (2017). Dependence of near field coseismic ionospheric perturbations on surface deformations: A case study based on the April, 25 2015 Gorkha, Nepal earthquake. *Advances in Space Research*, *59*(5), 1200–1208. https://doi.org/10.1016/j.asr.2016.11.041

Tsugawa, T., Saito, A., Otsuka, Y., Nishioka, M., Maruyama, T., Kato, H., … Murata, K. T. (2011). Ionospheric disturbances detected by GPS total electron content observation after the 2011 off the Pacific coast of Tohoku earthquake. *Earth, Planets and Space*, *63*(7), 875–879. https://doi.org/10.5047/eps.2011.06.035

Tulasi Ram, S., Su, S.-Y., Tsai, L.-C., & Liu, C. H. (2015). A self-contained GIM-aided Abel retrieval method to improve GNSS-radio occultation retrieved electron density profiles. *GPS Solutions*, *20*(4), 825–836. https://doi.org/10.1007/s10291-015-0491-z

Zettergren, M., & Snively, J. (2015). Ionospheric response to infrasonic-acoustic waves generated by natural hazard events. *Journal of Geophysical Research: Space Physics*, *120*(9), 8002–8024, https://doi.org/10.1002/2015JA021116

Zettergren, M. D., Snively, J. B., Komjathy, A., & Verkhoglyadova, O. P. (2017). Nonlinear ionospheric responses to large-amplitude infrasonic-acoustic waves generated by undersea earthquakes. *Journal of Geophysical Research: Space Physics*, *122*, 2272–2291. https://doi.org/10.1002/2016JA023159